communications materials

Article

https://doi.org/10.1038/s43246-024-00620-2

Atmospheric modulation of apparent electrical conductivity in a metal−organic framework

Yingchao Wang[1,2], Parker S. Brodale[3], Xiaohe Miao[4], Christopher H. Hendon[3] & Lei Sun[1,2,5] ✉

Combining high surface area and efficient charge transport, electrically conductive metal−organic frameworks (MOFs) find wide applications in energy storage, sensing, and electrocatalysis. Reliable characterization of electrical conductivity, the key metric for assessing this class of materials, remains challenging due to its high sensitivity to the atmosphere. Herein, through electrical characterization of an exemplary MOF, Cd_2(TTFTB) (TTFTB^{4-} = tetrathiafulvalene tetrabenzoate), under various controlled atmospheres, we show that adsorption of water in humid air or N_2 improves the apparent room-temperature electrical conductivity by one to two orders of magnitude compared to the values observed in dry atmospheres. This observation in conjunction with spectroscopic characterization, structural analysis, and band structure calculations indicates significant contribution of water-mediated proton conductivity and/or proton-electron coupling to the apparent electrical conductivity. Thus, controlling and reporting atmospheres in electrical conductivity measurements of MOFs is critical to improve their reproducibility and to gain insights into electrical conduction mechanisms.

Electrically conductive metal−organic frameworks (MOFs) are a unique class of materials that combine periodicity, microporosity, and electrical conductivity[1,2]. Recent advancements have led to MOFs with high electrical conductivity ($\sigma > 1000$ S·cm^{-1})[3,4], charge mobility ($\mu > 200$ cm^2·V^{-1}·s^{-1})[5], and charge density ($n > 1 \times 10^{21}$ cm^{-3})[6] at room temperature in conjunction with high Brunauer−Emmett−Teller surface area ($S_{BET} > 500$ m^2·g^{-1}). These properties have not only empowered exceptional performance of MOFs in a wide range of applications including supercapacitors[7], electrocatalysis[8], and chemiresistive sensing[9], etc., but also opened opportunities for investigating exotic physics[10] such as superconductivity[11–13], charge density wave[4], strong correlations[14], and topological insulators[15,16].

The development of electrically conductive MOFs demands sophisticated design of charge transport pathways and charge carriers, both of which require insights into structure−property relationships[2]. Accordingly, reliable data of crystal structures and electrical properties are indispensable to provide foundations for theoretical analysis on electronic band structures and charge transport mechanisms. The former has traditionally been acquired by bench-top X-ray diffraction (XRD) with high-quality large single crystals, while recent technological advances in continuous rotation electron diffraction (or microcrystal electron diffraction)[17,18] have enabled structural determination of sub-micrometer-scale single crystals with atomic resolution and precision. The structural data are typically reliable and reproducible: crystal structures of the same species reported by different laboratories are often nearly identical with marginal errors. In sharp contrast, there remain significant inconsistencies in the literature among reported electrical conductivity values of MOFs. For instance, the room-temperature electrical conductivity in an iconic MOF, Cu_3(HOTP)$_2$ (HOTP = 2,3,6,7,10,11-hexaoxytriphenylene), was reported to be on the order of 10^{-4} S·cm^{-1} or 0.02 S·cm^{-1} for thin films[19,20], 0.045 S·cm^{-1} or 0.1 S·cm^{-1} for pressed pellets[21,22], and 0.2 S·cm^{-1} or 1.5 S·cm^{-1} for single crystals[22,23]—it varies by one to several orders of magnitude. Such lack of consistency hinders the derivation of design principles for electrically conductive MOFs.

Reliable and reproducible characterization of electrical conductivity in MOFs is mainly limited by their morphologies, complex compositions, and microporous structures. First, the apparent electrical conductivity is highly dependent on the characterization method. Previous studies have revealed orders of magnitude variations in electrical conductivity values acquired from different device geometries (two-contact probe, four-contact probe, four-point, or van der Pauw geometries), crystallographic orientations

[1]Department of Chemistry, School of Science and Research Center for Industries of the Future, Westlake University, Hangzhou, 310030, China. [2]Institute of Natural Sciences, Westlake Institute for Advanced Study, Hangzhou, 310024, China. [3]Department of Chemistry and Biochemistry, Material Science Institute, University of Oregon, Eugene, OR, 97403, USA. [4]Instrumentation and Service Center for Molecular Sciences, Westlake University, Hangzhou, 310030, China. [5]Key Laboratory for Quantum Materials of Zhejiang Province, Department of Physics, School of Science, Westlake University, Hangzhou, 310030, China.
✉e-mail: sunlei@westlake.edu.cn

(perpendicular or parallel to charge transport pathways), and physical forms (thin films, pressed pellets, or single crystals)[22,24,25]. Second, it is difficult to fabricate high-quality electronic devices such as resistors, field-effect transistors, and Hall bars with single crystals of MOFs. The often small and irregularly shaped single crystals prevent fabrication of four-contact or van der Pauw devices by manually pasting electrical wires, and the lack of single crystalline thin films hinders the use of conventional micro/nano-fabrication technologies. Third, the complex components and microporous structures of MOFs make their electrical conductivity sensitive to the environment (atmosphere, temperature, illumination, etc.)[25–27]. Nonetheless, the environmental conditions are neither well controlled nor concretely described in many literatures, which significantly compromises the reproducibility of these reports.

Most electrical conductivity measurements of MOFs are conducted in three kinds of atmospheres: air, inert gas (nitrogen or argon), and vacuum. On one hand, the atmosphere may modulate structures of MOFs. Specifically, guest molecules may change coordination geometries of metal ions[28], $\pi-\pi$ stacking distances between conjugated ligands (*vide infra*), and even the shape of pores as exemplified by breathing MOFs[29]. Such structural modulation may alter energy match and orbital overlap among metal ions and organic ligands, leading to variation in electrical conductivity. On the other hand, components of the air, especially oxygen and water, could exert chemical influences on electrical conductivity when they are adsorbed into pores. The oxygen may introduce holes and quench electrons through oxidation reactions, leading to an increase in electrical conductivity of p-type semiconducting materials or a decrease in n-type ones[30]. The water may promote self-doping driven by proton-electron coupling[31] and may enable proton conduction[32–35]. Studying the dependencies of electrical conductivity on various components of the air would not only reveal insights into charge transport mechanisms but also help evaluate the potential of MOFs for chemiresistive sensing applications[9,36]. Therefore, it is critical to establish a methodology to articulate the atmospheric influence on electrical conductivity in MOFs.

Previously, we proposed a standard protocol on measuring and reporting electrical conductivity in MOFs by investigating the influence of characterization methods and environmental conditions on electrical conductivity in an exemplary MOF, Cd_2(TTFTB) ($TTFTB^{4-}$ = tetrathiafulvalene tetrabenzoate)[25]. Notably, single-crystal measurements under several cycles of evacuation and air-refilling at room temperature revealed an order of magnitude decrease in the electrical conductivity upon evacuation. Herein, we further investigated the atmospheric modulation of apparent electrical conductivity in Cd_2(TTFTB). Through structural, spectroscopic, and electrical characterizations under various atmospheres with controlled content of oxygen and water as well as electronic band structure calculations, we conclude that water, rather than oxygen, plays a key role in the air-induced improvement of the apparent electrical conductivity. Such improvement might stem from proton conductivity coupled with interfacial redox reactions and/or self-doping driven by proton-electron coupling. Thus, this study highlights the importance of controlling the atmosphere to improve reliability and reproducibility of electrical characterization for MOFs as well as to reveal insights into electrical conduction mechanisms.

Results and discussions

Structure and desolvation

Cd_2(TTFTB) was synthesized based on the previous literature (see Methods)[37]. Optical microscopy and scanning electron microscopy revealed hexagonal rod-like single crystals with regular shapes, millimeter-scale size, and smooth surfaces, which facilitate fabrication of single-crystal devices (Fig. 1d, e; Supplementary Fig. 1a). Single-crystal X-ray diffraction (SC-XRD) of the as-synthesized Cd_2(TTFTB) revealed π-stacked TTF columns formed by $\pi-\pi$ stacking and S···S interactions between TTF moieties along the crystallographic *c*-axis (Fig. 1b). The side chain consists of two alternating and crystallographically independent Cd^{2+} ions bridged by carboxylate groups (Fig. 1c). One type of Cd^{2+} is six-coordinated and is bound to two terminal water molecules; the other type is five-coordinated and does not coordinate to water. The π-stacked TTF columns and side chains together delineate one-dimensional (1D) quasi-elliptic cylindrical pores (Fig. 1a). This structure is different from the previously reported Cd_2(TTFTB)[37] yet analogous to several other M_2(TTFTB) (M = Mn^{2+}, Co^{2+}, and Zn^{2+})[37,38]. SC-XRD showed solvent molecules in the pores and elemental analysis revealed a formula of $[Cd_2(TTFTB)(H_2O)_2]\cdot(DMF)_{1.34}(H_2O)_{3.73}$ (DMF = *N*,*N*-dimethylformamide). The guest DMF and water molecules may assist with the terminal water molecules to form hydrogen-bonded networks within the pores.

Electrical characterization of Cd_2(TTFTB) involves maintaining its crystal in the air at temperature up to 363 K and relative humidity (RH) up to 90% or purging it in dry N_2 for 1 h at a fixed temperature that varies from 298 K to 363 K (see Methods). The structural stability of Cd_2(TTFTB) under elevated temperature and humidity was confirmed by powder X-ray diffraction (PXRD), which revealed consistent diffraction pattern after subjecting crystals to the air at 353 K and 90% RH for 72 h (Fig. 1f; Supplementary Figs. 2 and 3). The diffraction angles and widths of PXRD peaks persisted after this treatment, confirming the integrity of the framework structure.

We further investigated the desolvation of Cd_2(TTFTB) with thermogravimetric analysis coupled with Fourier transform infrared spectroscopy (TGA-FTIR). To simulate the electrical characterization procedures, the sample was heated slowly to 363 K in a flow of dry N_2, maintained at this temperature for 1 h, and heated rapidly to 473 K. TGA shows a mass loss during the whole treatment, which is attributed to desolvation (Supplementary Fig. 4). In the first two stages, the degas rate was too slow to meet the detection limit of spectrometer, resulting in negligible features of water or DMF in IR spectra (Fig. 1g). In contrast, rapid degassing took place during the fast-heating stage, revealing intense IR features of DMF (e.g., C = O stretch at approximately 1700 cm^{-1}) as well as a weak and broad band centered at approximately 3400 cm^{-1} that signifies water. The former shows up at above 417 K that is comparable to the boiling point of DMF (426 K), whereas the latter was only observed at 473 K that is much higher than the boiling point of water (373 K) likely due to a strong binding of water to Cd^{2+}. Thus, the N_2 purging process involved in electrical characterization desolvates Cd_2(TTFTB) partially—only a portion of DMF and water may be removed from the pores.

DC electrical characterization

Two-contact probe single-crystal devices of Cd_2(TTFTB) were fabricated to characterize the electrical conductivity along the crystallographic *c*-axis (Fig. 2a and Supplementary Fig. 1b). To elucidate the atmospheric modulation of electrical conductivity in Cd_2(TTFTB), we conducted direct-current (DC) electrical characterization at room temperature (298 K) and under various atmospheres including humid air (38% − 45% RH), humid N_2 (100% RH), dry air (<2% RH), and dry N_2 (<0.02% RH) (Supplementary Fig. 1c). The comparison between humid and dry atmospheres reveals the influence of water on the DC conductivity, whereas that between air and N_2 atmospheres shows the influence of oxygen (Fig. 2b). Current−voltage (I − V) curves are linear in all tested atmospheres, allowing extraction of the apparent electrical conductivity values with the Ohm's law (Fig. 2c).

For a representative device, the DC conductivity in humid air is $\sigma_{DC,\ humid\ air} = 9.44 \times 10^{-5}$ S·cm^{-1}, which is consistent with previously reported values of Cd_2(TTFTB)[25,37]. The crystal was then purged in dry N_2 at 363 K for 1 h to desolvate it, cooled down to 298 K, maintained in dry N_2 for 1 h, and exposed to dry air for 1 h (see details in Methods and Supplementary Fig. 5). As discussed above, this treatment can only desolvate the framework partially with a significant amount of residual DMF and coordinating water in pores. Nonetheless, it reduced the DC conductivity to $\sigma_{DC,\ dry\ N2} = 1.03 \times 10^{-6}$ S·cm^{-1}, which remained in dry air ($\sigma_{DC,\ dry\ air} = 1.06 \times 10^{-6}$ S·cm^{-1}). Finally, exposing the crystal to humid N_2 for 1 h improved the DC conductivity to $\sigma_{DC,\ humid\ N2} = 5.24 \times 10^{-5}$ S·cm^{-1}. This is slightly lower than $\sigma_{DC,\ humid\ air}$, which may be attributed to desolvation-induced changes of the crystal structure (*vide infra*) and guest composition in pores. Nonetheless,

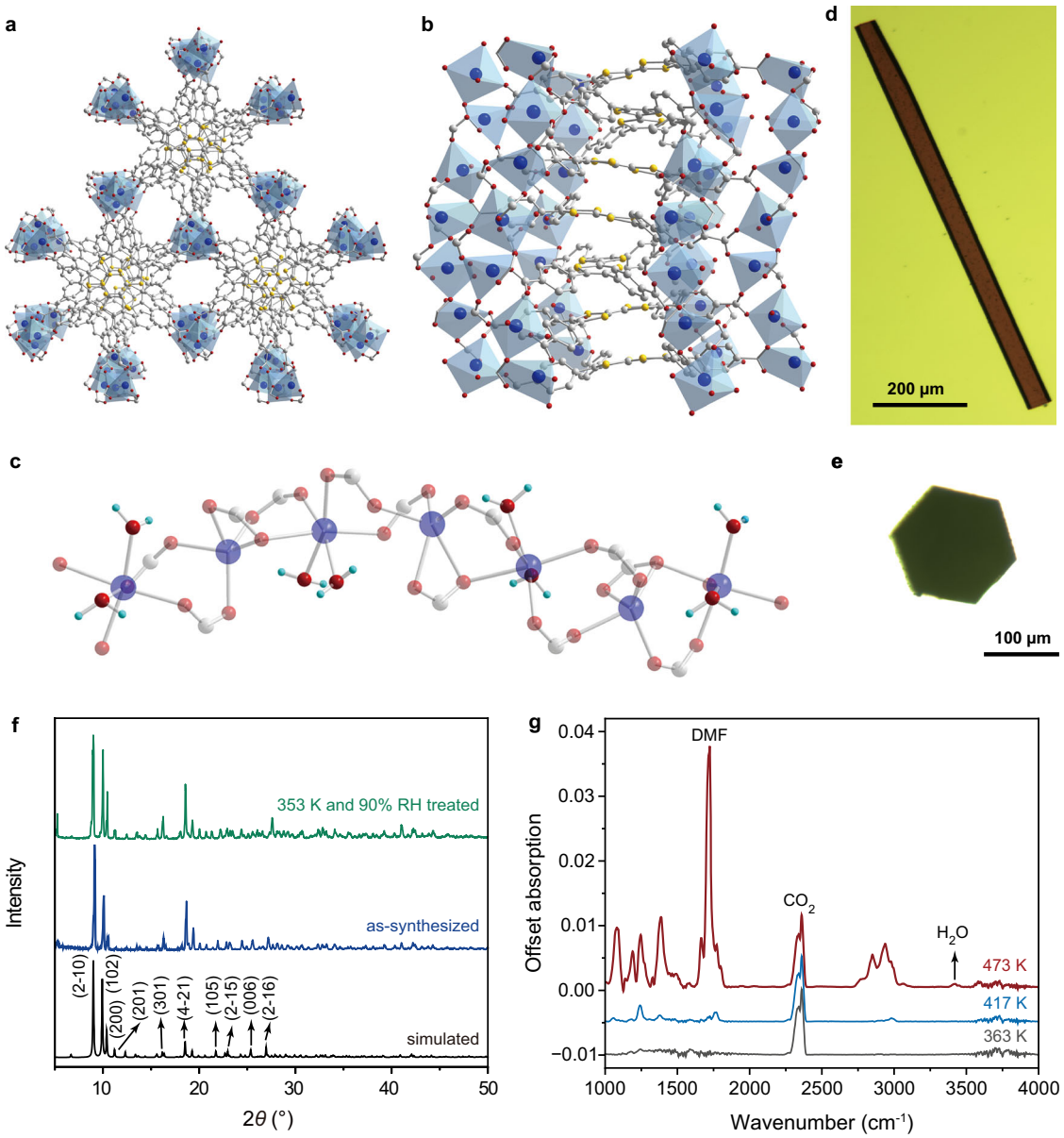

Fig. 1 | Structure and desolvation of Cd_2(TTFTB). a, **b** Portions of structures viewed parallel or perpendicular to the crystallographic *c*-axis showing nanoscale pores or the π-stacked TTF columns, respectively. Gray, red, yellow, and purple spheres represent C, O, S, and Cd, respectively. Solvent and H atoms are omitted for clarity. **c** Portion of the side chain highlighting terminal water molecules. **d**, **e** Micrographs of single crystals viewed perpendicular or parallel to the long axis, respectively. **f** PXRD patterns of the as-synthesized Cd_2(TTFTB) and a sample treated at 353 K and 90% RH for 72 h in comparison with a pattern simulated from the crystal structure. Miller indices of primary PXRD peaks are indicated. **g** IR spectra of evaporated gaseous products generated at various temperatures from TGA. IR features of CO_2 appeared due to instrumental artefacts.

such recovery indicates that the low DC conductivity values under dry atmospheres were not caused by an accidental device damage. Thus, the room-temperature DC conductivity of Cd_2(TTFTB) shows the following trend: $\sigma_{DC,\ humid\ air} > \sigma_{DC,\ humid\ N2} \gg \sigma_{DC,\ dry\ air} \approx \sigma_{DC,\ dry\ N2}$ (Fig. 2d).

We further conducted variable-atmosphere DC electrical characterization for crystals from different batches and N_2-purged at 298 K. The order of atmospheres was switched for some devices and two cycles of measurements were performed for one device. Characterization of four-contact probe single-crystal devices was also conducted to eliminate the influence of contact resistance (Supplementary Fig. 1d). Although the exact electrical conductivity values differ among these devices, their atmospheric dependencies are consistent with the above trend (see examples in Supplementary Figs. 6 and 7). In addition, we monitored dynamic changes of the current through a device (Fig. 2e and Supplementary Fig. 8). Purging the single crystal of Cd_2(TTFTB) with dry N_2 reduced the current immediately, reaching a plateau after 700 s. Switching dry N_2 to dry air caused a negligible change in current. We then switched the purging gas to humid N_2. The current first slightly dropped for 70 s, then increased sharply, and finally levels off after 900 s. Notably, both the decline of current in dry N_2 and the rise of current in humid N_2 exhibit exponential decays with rate constants of 0.126 s^{-1} and 0.019 s^{-1}, respectively (Supplementary Fig. 9). These trends are consistent with the first-order dynamics of desorption and adsorption[39]. Thus, the adsorbed guests should play a major role in the variation of electrical conductivity.

Atmospheric modulation of charge mobility and hole density

The DC electrical conductivity is a product of elementary charge (e), charge mobility (μ), and charge density (n), i.e., $\sigma = e\mu n$[2]. Therefore, it is viable to examine charge mobility and charge density separately to understand their modulation by the atmosphere.

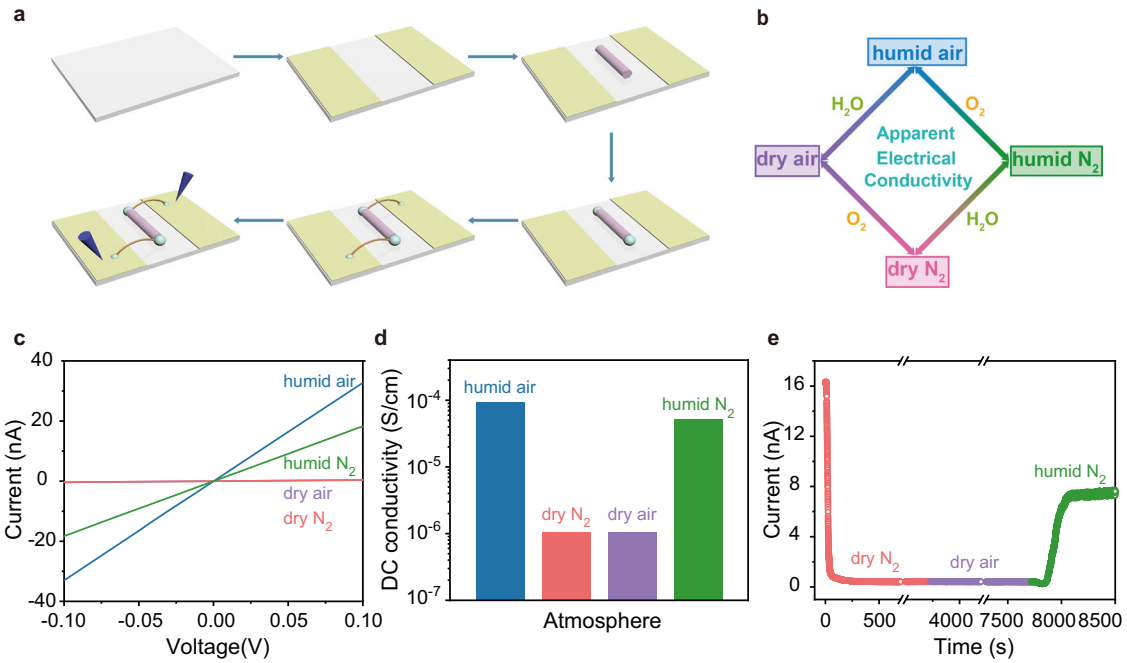

Fig. 2 | DC electrical characterization and analysis of Cd_2(TTFTB). a Fabrication of a single-crystal two-contact probe device. Pink, pale green, orange, yellow, gray, and blue objects represent a single crystal of Cd_2(TTFTB), carbon paste, gold wires, gold electrodes, a piece of glass slide, and electrical probes, respectively. **b** Protocol for elucidating the influence of O_2 and H_2O on the apparent electrical conductivity with variable-atmosphere electrical characterization. **c** I − V curves acquired at 298 K under humid air, humid N_2, dry air, and dry N_2, where the latter two overlap under the scale of this figure. **d** Comparison of the DC conductivity in different atmospheres. **e** Dynamic variation of the electrical current through a device under an applied bias of 0.1 V in various atmospheres.

Directly measuring the charge mobility of Cd_2(TTFTB) is challenging due to technical difficulties of fabricating field-effect transistors or Hall bars. Hence, we probed it indirectly with structural characterization. Previous studies on a series of M_2(TTFTB) (M^{2+} = Mn^{2+}, Co^{2+}, Zn^{2+}, Cd^{2+}) materials showed that their electrical conductivity increases with decreasing S···S distances. This was rationalized by enhanced overlap between $3p_z$ orbitals of adjacent TTF moieties and in turn improved charge mobility[37,38]. As the S···S contact is in line with the crystallographic *c*-axis, a shorter S···S distance should manifest as a reduced unit cell parameter in the *c* direction.

Driven by this hypothesis, we conducted in situ PXRD measurements on Cd_2(TTFTB) using $CaCO_3$ as an internal reference for calibration (Supplementary Fig. 10). The PXRD patterns were analyzed by the Le Bail refinement to extract unit cell parameters (Supplementary Figs. 11−15). A PXRD pattern of the as-synthesized Cd_2(TTFTB) was first acquired in humid air, revealing unit cell parameters of $a = b = 19.6463$ Å and $c = 21.0196$ Å, which are consistent with those obtained from SC-XRD (Supplementary Table 1). The same sample was then evacuated at 298 K for 1 h. Its PXRD peaks shifted towards high angles with the most representative (006) diffraction peak shifting from 25.39° to 25.96° (Fig. 3b, c). Although the crystal symmetry remained, the evacuation caused a contraction of the unit cell to $a = b = 19.5446$ Å and $c = 20.5834$ Å. The sample was then allowed to stay in the humid air for 1 h, which shifted the PXRD peaks back towards low angles. The (006) diffraction peak was at 25.52°, and the unit cell parameters were $a = b = 19.6411$ Å and c = 20.8910 Å. This unit cell is slightly smaller than that of the as-synthesized sample, which is likely due to partial removal of the adsorbed solvent (*vide supra*). The evacuation and air-refilling process was repeated once, displaying nearly consistent PXRD patterns with the (006) peak showing at a slightly higher angle possibly due to further removal of solvent during the second evacuation process. These observations indicate that the S···S distance decreases because of partial desolvation, which should lead to an increase in charge mobility.

To confirm the shortening of the S···S distance, we evacuated Cd_2(TTFTB) at room temperature for 15 h and acquired its crystal structure by SC-XRD. This treatment removed the adsorbed solvent and shrank the unit cell to $a = b = 19.6184$ Å and $c = 20.6160$ Å (Supplementary Table 2), matching well with the parameters obtained from PXRD. Importantly, the S···S distance decreases from 3.71 Å in the as-synthesized framework to 3.62 Å in the evacuated one (Fig. 3d, e). Density functional theory (DFT) calculations were performed on both the as-synthesized and evacuated forms of Cd_2(TTFTB) (Fig. 3f, g), revealing nearly identical electronic band features. Aligning with the previous report[37], the valence band maximum is a six-folded carbon and sulfur band (Γ–A) with a bandwidth of 293 meV for the as-synthesized material. Evacuation results in contraction in the π-stacked TTF column by approximately 3%, which is quantitatively consistent with the experimentally observed contraction, and a corresponding increase in the bandwidth to 333 meV due to the increased S $3p_z$-orbital overlap. Since TTF is a hole acceptor[40] and the curved bands are associated with the π-stacked TTF columns, both forms of Cd_2(TTFTB) should behave as p-type semiconductors. The increase in valence band curvature should lead to a reduction of hole effective mass and an enhancement of hole mobility.

Cd_2(TTFTB) is known to contain TTF^{+} radical cations[37], which are likely formed through spontaneous oxidation of the TTF moiety by O_2 during the high-temperature synthesis of the precursor or framework. If the relatively high $\sigma_{DC,\ humid\ air}$ had been caused exclusively by TTF oxidation, the concentration of TTF^{+} radical cations would be significantly higher in aerobic atmospheres than that in anaerobic atmospheres. To investigate this possibility, we conducted continuous wave electron paramagnetic resonance (CW-EPR) spectroscopic characterization on the same sample of Cd_2(TTFTB) under both aerobic and evacuated conditions at 298 K. Both CW-EPR spectra exhibit single axial peaks with $g_{\parallel}$ and $g_{\perp}$ centered at 2.0068 and 2.0013, respectively (Fig. 3a). These are close to the free electron value ($g = 2.0023$), confirming the presence of TTF^{+}. Notably, the evacuation barely changes the concentration of radicals as indicated by nearly identical peak intensities and shapes in the two spectra. Thus, the presence of O_2 does not promote further oxidation of Cd_2(TTFTB) at room temperature and in turn does not improve the hole density. This is consistent with the above-mentioned observation that $\sigma_{DC,\ dry\ air} \approx \sigma_{DC,\ dry\ N2}$.

Therefore, upon evacuating Cd_2(TTFTB), its charge mobility increases, and its charge density persists, which together should enhance the

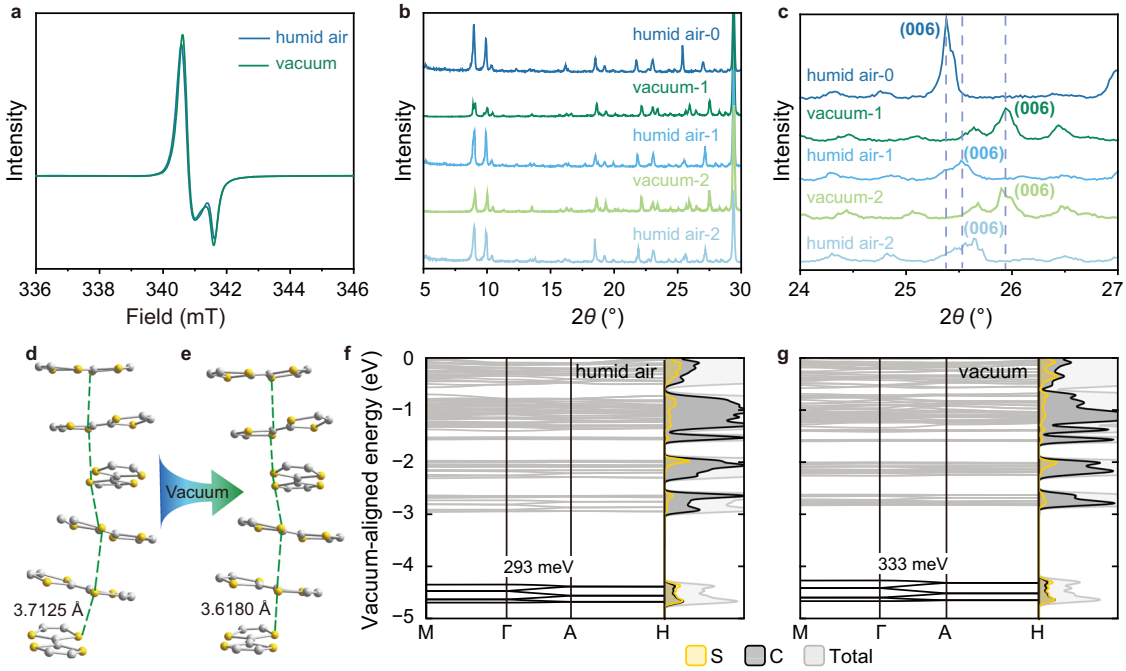

Fig. 3 | Atmospheric modulation of charge mobility and charge density of Cd_2(TTFTB). a CW-EPR spectra collected in humid air and in vacuum. **b** in situ PXRD patterns collected in humid air (process 0) and then during two cycles of evacuation and air-refilling treatment (process 1 and 2). Patterns were calibrated by the $CaCO_3$ standard (the intense peak at 29.4°). **c** in situ PXRD patterns zoomed at the region of (006) diffraction. Dashed lines are to guide eyes. **d** π-stacked TTF columns in the as-synthesized and **e** evacuated Cd_2(TTFTB) highlighting the shortest S···S contact. **f**, **g** Electronic band structures of the as-synthesized and evacuated frameworks. M–Γ and A–H are in-plane vectors, while Γ–A samples the TTF π-stacking direction.

electrical conductivity. Although technical limitations prevented us from performing these measurements in dry N_2, the same trend is expected as dry N_2 purging also removes portions of guest molecules. This is contrary to the experimental observation that $\sigma_{DC,\ humid\ air} \gg \sigma_{DC,\ dry\ N2}$. It implies that in humid air, besides $TTF^{\cdot+}$-based hole conduction, other charge transport mechanisms and/or charge carriers are involved, which are likely mediated by coordinating water and adsorbed solvent molecules.

AC electrical characterization

To investigate the contribution of water to apparent electrical conductivity in Cd_2(TTFTB), we performed alternative-current (AC) electrochemical impedance spectroscopy (EIS) and DC I − V measurements, which reveal AC and DC conductivity, respectively, for the same device at 298 K under humid air, humid N_2, dry air, and dry N_2. The Nyquist plot obtained from EIS characterization under each atmosphere appears to be a semicircle. It can be well fitted by an equivalent parallel circuit consisting of a resistor and a capacitor. The resistance was used to calculate the AC conductivity (Supplementary Fig. 16)[32]. In each atmosphere, the AC and DC conductivity values are nearly identical — they differ by less than 1%. Take the above-mentioned single-crystal device for example. Its AC conductivity in humid air was $\sigma_{AC,\ humid\ air} = 9.38 \times 10^{-5}$ S·cm^{-1}, dropped to $\sigma_{AC,\ dry\ air} = 1.06 \times 10^{-6}$ S·cm^{-1} in dry air and $\sigma_{AC,\ dry\ N2} = 1.03 \times 10^{-6}$ S·cm^{-1} in dry N_2, and recovered to $\sigma_{AC,\ humid\ N2} = 5.26 \times 10^{-5}$ S·cm^{-1} in humid N_2 (Fig. 4a, b). These values match closely with DC counterparts (Fig. 2d).

We further conducted EIS and DC I − V measurements for several devices at 298 K and in the air with the relative humidity ranging from 20% RH to 90% RH. Both AC and DC conductivity values increase exponentially with increasing relative humidity, and they match well with each other (Fig. 4c and Supplementary Fig. 17). For instance, in an exemplary device, both started with 1.31×10^{-4} S·cm^{-1} at 20% RH and rose to 1.75×10^{-4} S·cm^{-1} at 90% RH. Extrapolating the conductivity value to 0% RH gives 1.30×10^{-4} S·cm^{-1}, which is significantly higher than the expected value in dry air and dry N_2 likely because the material was desolvated to a higher degree in these dry atmospheres. These observations confirm the key role of water in the apparent electrical conduction. Hence, we tentatively assigned the AC conductivity to proton conductivity. Considering the ratio between $\sigma_{humid\ air}$ and $\sigma_{dry\ air}$ observed from both DC and AC electrical characterization, the proton conductivity is at least 1 − 2 orders of magnitude higher than the electrical conductivity in humid atmospheres.

Electrical conduction mechanisms

Water may contribute to the apparent electrical conduction in Cd_2(TTFTB) through two mechanisms. On one hand, water could provide protons and help form their conduction pathways[32]. Meanwhile, although the TTF moiety is not oxidized by the air at room temperature, it could undergo redox reactions at the crystal−electrode interface under an applied electric field, giving rise to so called interfacial pseudo-capacitance[41]. The coupling between proton conductivity and interfacial pseudo-capacitance may improve the apparent electrical conductivity value, resulting in an overestimation of the latter (Fig. 4d). This phenomenon has been observed in $[(CH_3)_2NH_2]In(H_4TTFOC)$ (H_8TTFOC = tetrakis(3,5-dicarboxyphenyl)-tetrathiafulvalene) in which proton conduction and interfacial redox reactions of the TTF moiety improve the apparent DC conductivity by five orders of magnitude[41]. On the other hand, water could be deprotonated under an applied electric field, which facilitates the formation of holes through proton-electron coupling. Such self-doping process improves hole density and thereby electrical conductivity, as evident by molecular conductors comprising of TTF moieties and protonic functional groups (e.g., hydroxy)[31,42,43].

Both mechanisms require redox-active components and hydrogen-bonded networks. Although there are terminal water molecules in the structure, their locations and orientations prevent direct formation of long-range hydrogen-bonded networks (Fig. 1c). This explains the relatively low DC and AC conductivity in dry atmospheres. These distant coordinating water molecules might be connected by adsorbed water and DMF to form hydrogen-bonded networks in the pores to promote proton conduction[41,44]. The proton conduction may couple with interfacial redox reactions of TTF moieties to contribute to the DC conductivity[41]. Meanwhile, such hydrogen-

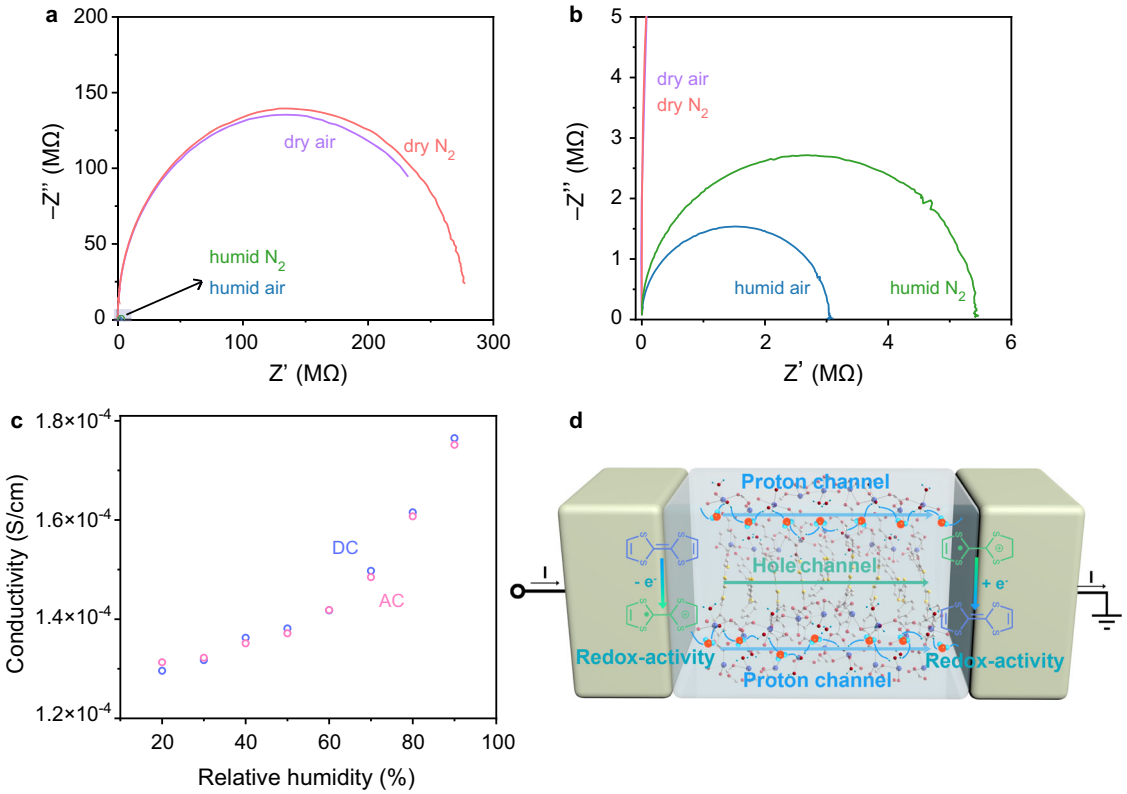

Fig. 4 | AC electrical characterization of Cd_2(TTFTB). a, **b** Nyquist plots acquired at 298 K under various atmospheres. **c** DC and AC conductivity acquired at 298 K under various relative humidities for the same device. **d** Schematic illustration of the hole transport pathway and the proton conduction channel coupled with redox reactions at the crystal−electrode interface.

bonded networks could also promote self-doping that improves hole-based electrical conduction through π−stacked TTF columns. The latter is unlikely to be dominant because non-conjugated linkages (e.g., Cd^{2+}−carboxylate coordination) between hydrogen-bonded networks and TTF columns should lead to weak proton-electron coupling. Although contributions differ, both mechanisms may be applicable to Cd_2(TTFTB), rendering it as a potential candidate of proton−electron dual conductor (Fig. 4d)[45,46].

Conclusions

In conclusion, electrical, spectroscopic, structural characterization and band structure calculations of an exemplary MOF, Cd_2(TTFTB), revealed that water molecules in the atmosphere could modulate its apparent electrical conductivity by 1 – 2 orders of magnitude. Cd_2(TTFTB) has long been perceived as a p-type semiconductor[25,37], yet our studies indicate that its apparent electrical conductivity likely manifests a combination of electrical conduction through π-stacked TTF columns and proton conduction through hydrogen-bonded networks. Both are promoted by the redox activity of TTF moieties and protons provided by coordinating water and adsorbed solvent. This finding raises demands on elucidating the underlying mechanism of apparent electrical conductivity in MOFs, especially those that lack electron/hole transport pathways but comprise of redox-active building blocks and potential proton sources (e.g., coordinating water and carboxylic acid groups).

As various components of the air (H_2O, O_2, CO_2, N_2, etc.) could affect charge transport pathways, charge densities, and types of charge carriers, the atmospheric modulation is expected to take place in a wide range of MOFs. Without controlling the atmosphere of electrical conductivity measurements, it is difficult to achieve consistent results even for the same batch of materials and to reproduce the results reported by other laboratories. Meanwhile, conducting electrical characterization under a well-controlled atmosphere allows probing the influence of a specific gas molecule on the electrical conductivity, which may bring insights into the electrical conduction mechanism as shown herein and portend applications of the framework for chemiresistive sensing. Thus, we suggest subsequent studies on the electrical conductivity in MOFs to record, control, and report the characterization atmosphere to improve reliability, verifiability, and reproducibility, ultimately establishing a unified standard for the field of electrically conductive MOFs.

Methods

Synthesis of Cd_2(TTFTB)

Cd_2(TTFTB) was synthesized by modifying the previous reported procedure[37]. $Cd(NO_3)_2{\cdot}4H_2O$ (172 mg, 0.558 mmol) was dissolved in a mixture of 6 mL water and 6 mL ethanol. H_4TTFTB (103 mg, 0.154 mmol) was dissolved in 6.3 mL DMF and 2.1 mL ethanol in a 20 mL scintillation vial. Both solutions were sonicated for 3 min. The former solution was slowly added to the latter with a pipette, and the mixture was sonicated for 3 min. The reaction mixture was heated to 75 °C in 10 h in a programmable oven, kept at this temperature for 72 h, and cooled down to 30 °C in 10 h, affording dark red rod-like crystals. The top solution was decanted. The remaining crystals were washed by soaking them in DMF for 3 times and then in ethanol for 3 times. Finally, the product was dried in a vacuum oven at 40 °C for 24 h. Elemental analysis calcd. For $C_{38}H_{36.8}N_{1.34}O_{15.1}S_4Cd_2$: C, 41.26; H, 3.36; N, 1.70; Found: C, 41.23; H, 3.24; N, 1.75.

Fabrication of single-crystal devices

A single crystal with a smooth surface and regular rod-like shape was selected under an optical microscope (Guangzhou Liss Optical Instrument L3230) equipped with a digital camera (LIT Firefly 12). The crystal was then transferred onto a piece of glass slide. The glass slide was pre-patterned with two electrodes fabricated by depositing 5 nm Ti and 60 nm Au with an e-beam evaporator (ULVAC ei-5z) using a piece of Kapton tape as a shield mask. A gold wire was attached to one end of the rod-like crystal with carbon

paste, and the other end of the gold wire was subsequently connected to the gold electrode with carbon paste. The same procedure was repeated on the other end of the crystal to fabricate a single-crystal two-contact probe device with electrical current transporting along the crystallographic *c*-axis (Fig. 2a). Single-crystal four-contact probe devices were fabricated by pasting another two wires in the middle of the crystal. The length and edge of cross-section of the conduction channel were measured by the optical microscope and a digital camera.

DC I − V and EIS characterization

Single-crystal two-contact probe devices were used without further specification. The device was placed in a mini electrical probe stage (INSTEC HP1000G-PM) capable of accommodating various atmospheres and temperatures. A probe was brought into contact with each gold electrode. Electrical characterization was conducted at room temperature (298 K). DC I − V curves were acquired with the Current Voltage Curves (Steady State) module of a potentiostat (Zahner Zennium Pro) or with a sourcemeter (Keithley 2636B). Voltage was scanned from −0.1 V to 0.1 V with a step size of 1 mV while the current was collected at each step. The DC resistance (R_{DC}) was extracted by linear fitting of the I − V curve according to the Ohm's law. EIS measurements were conducted with the Potentiostatic module of the potentiostat (Zahner Zennium Pro). The amplitude of AC voltage was kept at 500 mV and the frequency was scanned from 8 MHz to 1 Hz. The obtained Nyquist plot was fitted by an equivalent parallel circuit containing a resistor and a capacitor:

$$(Z' - \frac{R_{AC}}{2})^2 + Z''^2 = (\frac{R_{AC}}{2})^2$$

where Z' and Z" represent the real and imaginary components of impedance, respectively, and R_{AC} represents the AC resistance. The apparent electrical conductivity (σ_{DC}) and proton conductivity (σ_{AC}) were calculated by taking the geometry of conduction channel into account[25]:

$$\sigma_{DC} = \frac{1}{R_{DC}} \times \frac{2\sqrt{3}L}{9E^2} \text{ and } \sigma_{AC} = \frac{1}{R_{AC}} \times \frac{2\sqrt{3}L}{9E^2}$$

Variable-atmosphere σ_{DC} and σ_{AC} measurements were conducted with the following process. First, $\sigma_{DC,\ humid\ air}$ and $\sigma_{AC,\ humid\ air}$ were acquired in humid air. The probe station chamber was then purged by dry N_2. The device was either kept at 298 K for 1 h, or it was heated to an elevated temperature with a rate of 0.8 °C/min. This heating rate was chosen to avoid crystal fracturing. The crystal was then kept at that temperature for 1 h and cooled down to 298 K with the same rate. $\sigma_{DC,\ dry\ N2}$ and $\sigma_{AC,\ dry\ N2}$ were then acquired, followed by purging the chamber with dry air at 298 K for 1 h and measuring $\sigma_{DC,\ dry\ air}$ and $\sigma_{AC,\ dry\ air}$. Finally, the chamber was purged by humid N_2 at 298 K for 1 h and both $\sigma_{DC,\ humid\ N2}$ and $\sigma_{AC,\ humid\ N2}$ were measured. The humid N_2 was prepared by flowing dry N_2 through deionized water at 298 K.

Variable-humidity σ_{DC} and σ_{AC} measurements were conducted after maintaining the device in the air at 298 K and each relative humidity for 30 min. The relative humidity was controlled using a humidity and temperature control chamber (Doaho, DHTLH-27). The device was kept inside this chamber was connected to the potentiostat or sourcemeter through two Teflon-covered electrical wires.

TGA-FTIR characterization

Thermogravimetry analyzer coupled with Fourier Transform Infrared spectrometer (TGA8000/Spectrum 3, Perkin-Elmer, the UK) was used for acquiring the real-time information about the quantity and type of the gaseous functional groups. The sample was heated from 25 °C to 90 °C with a heating rate of 0.8 °C/min, maintained at 90 °C for 60 min, and then heated to 200 °C with a heating rate of 25 °C/min. The first two processes simulated experimental procedures involved in electrical characterization, and the last process produced fast degassing from the sample. Dry N_2 at a flow rate of 30 mL/min carried the evolved gas products through a stainless steel line into the gas cell for IR detection. The transfer line, adapter, and the FTIR gas cell were kept at 100 °C to avoid gas condensation. IR spectra were recorded in the spectral range of 4000 − 600 cm^{-1} with a resolution of 8 cm^{-1} and 8 scans.

CW EPR characterization

Crystals of as-synthesized Cd_2(TTFTB) were added into a quartz tube. The CW EPR spectrum was acquired at 298 K using a CIQTEK EPR200M spectrometer operating at X-band (9.6 GHz) frequencies. The modulation amplitude was set to 2.0 Gauss and the microwave power was 0.1 mW. The same sample was then flame sealed in vacuum with a vacuum tube sealer (BALAB MRVS1003S003). Its CW EPR spectrum was acquired with the same instrument and parameters.

SC-XRD characterization

X-ray diffraction measurement for Cd_2(TTFTB) compounds was collected at 305(2) K, performed on a Bruker D8 Venture diffractometer with PHOTON III detector in shutterless mode with an incoatec microfocus source (Mo-Diamond Kαradiation, λ = 0.71073 Å) and an Oxford 800 Plus liquid nitrogen vapor cooling device. Details of sample preparation, data analysis, and structural determination are presented in the Supplementary Information. Asymmetric units, crystal data, data collection parameters, and structure refinement details of the as-synthesized Cd_2(TTFTB) are given in Supplementary Fig. 18 and Table 1, and those of the evacuated Cd_2(TTFTB) are given in Supplementary Fig. 19 and Table 2.

in situ PXRD characterization

in situ PXRD characterization was conducted with Bruker D8 Discover diffractometer equipped with a θ/2θ Bragg-Brentano geometry, a rotational Cu anode (6 kW TXS-HE X-ray source), and a 2D Eiger detector. The tube voltage and current were 42 kV and 100 mA, respectively. The 2θ angle was scanned from 5° to 50° with a step size of 0.02° and a scan rate of 0.3 s per step. The sample was prepared by grinding crystals of Cd_2(TTFTB) (50 mg) and the $CaCO_3$ standard (50 mg) in a mortar for 10 min. A portion of the mixture was used to fill an XRD non-ambient stage (MTC-LOWTEMP), and its PXRD pattern was acquired in humid air (temperature: 296–298 K; relative humidity: 40 − 45%). The sample was evacuated at 10^{-2} mbar and 298 K for 1 h, and it was exposed to humid air for 1 h. PXRD patterns were taken at the end of each process. This procedure was repeated once. Le Bail refinement of the PXRD pattern was performed by TOPAS.

Electronic band structure calculations

Beginning with the experimentally determined single crystal structures, the materials were geometrically equilibrated within VASP using the PBEsol[47] functional paired with a 500 eV cutoff, a 2 × 2 × 2 k-grid, and an ionic convergence of less than 0.005 eV per atom. The electronic band structures were then computed using the same functional, and the band gap was adjusted to the computed HSEsol[48] gap at the Γ-point, using the same basis. The band structures were aligned to vacuum using a prior method[49].

Data availability

The crystallographic information has been deposited in the Cambridge Crystallographic Data Center (CCDC) under accession codes 2372942 and 2372943. All data supporting the findings of this study are available within the paper and its Supplementary Information.

Received: 31 March 2024; Accepted: 21 August 2024;
Published online: 29 August 2024

References

1. Li, W.-H., Deng, W.-H., Wang, G.-E. & Xu, G. Conductive MOFs. *EnergyChem* **2**, 100029 (2020).
2. Xie, L. S., Skorupskii, G. & Dincă, M. Electrically conductive metal–organic frameworks. *Chem. Rev.* **120**, 8536–8580 (2020).

3. Huang, X. et al. A two-dimensional π–d conjugated coordination polymer with extremely high electrical conductivity and ambipolar transport behaviour. *Nat. Commun.* **6**, 7408 (2015).
4. Skorupskii, G. et al. Porous lanthanide metal–organic frameworks with metallic conductivity. *Proc. Natl. Acad. Sci* **119**, e2205127119 (2022).
5. Dong, R. et al. High-mobility band-like charge transport in a semiconducting two-dimensional metal–organic framework. *Nat. Mater.* **17**, 1027–1032 (2018).
6. Lu, Y. et al. Tunable charge transport and spin dynamics in two-dimensional conjugated meta–organic frameworks. *J. Am. Chem. Soc* **146**, 2574–2582 (2024).
7. Niu, L. et al. Conductive metal–organic frameworks for supercapacitors. *Adv. Mater.* **34**, 2200999 (2022).
8. Dou, S., Li, X. G. & Wang, X. Rational design of metal–organic frameworks towards efficient electrocatalysis. *ACS Mater. Lett.* **2**, 1251–1267 (2020).
9. Park, C., Baek, J. W., Shin, E. & Kim, I.-D. Two-dimensional electrically conductive metal–organic frameworks as chemiresistive sensors. *ACS Nanosci. Au* **3**, 353–374 (2023).
10. Wang, S., Wang, Y., Sun, H. & Sun, L. Emergent physics in metal −organic frameworks. *Chin. J. Chem.* **42**, 2514–2519 (2024).
11. Huang, X. et al. Superconductivity in a copper(II)-based coordination polymer with perfect kagome structure. *Angew. Chem. Int. Ed.* **57**, 146–150 (2018).
12. Takenaka, T. et al. Strongly correlated superconductivity in a copper-based metal–organic framework with a perfect kagome lattice. *Sci. Adv.* **7**, eabf3996 (2021).
13. Pan, Z. et al. Atomic-precision non-van der waals 2D structures: superconductivity in π-d conjugated coordination polymers. *ChemRxiv* https://doi.org/10.26434/chemrxiv-2024-296c0 (2024).
14. Perlepe, P. et al. From an antiferromagnetic insulator to a strongly correlated metal in square-lattice $MCl_2(pyrazine)_2$ coordination solids. *Nat. Commun.* **13**, 5766 (2022).
15. Wang, Z. F., Liu, Z. & Liu, F. Organic topological insulators in organometallic lattices. *Nat. Commun.* **4**, 1471 (2013).
16. Jiang, W., Ni, X. & Liu, F. Exotic topological bands and quantum states in metal–organic and covalent–organic frameworks. *Acc. Chem. Res.* **54**, 416–426 (2021).
17. Huang, Z., Grape, E. S., Li, J., Inge, A. K. & Zou, X. 3D electron diffraction as an important technique for structure elucidation of metal–organic frameworks and covalent organic frameworks. *Coordin. Chem. Rev.* **427**, 213583 (2021).
18. Yang, T., Willhammar, T., Xu, H., Zou, X. & Huang, Z. Single-crystal structure determination of nanosized metal–organic frameworks by three-dimensional electron diffraction. *Nat. Protoc.* **17**, 2389–2413 (2022).
19. Rubio-Giménez, V. et al. Bottom-up fabrication of semiconductive metal–organic framework ultrathin films. *Adv. Mater.* **30**, 1704291 (2018).
20. Yao, M.-S. et al. Layer-by-layer assembled conductive metal–organic framework nanofilms for room-temperature chemiresistive sensing. *Angew. Chem. Int. Ed.* **56**, 16510–16514 (2017).
21. Hoppe, B. et al. Graphene-like metal–organic frameworks: morphology control, optimization of thin film electrical conductivity and fast sensing applications. *CrystEngComm* **20**, 6458–6471 (2018).
22. Day, R. W. et al. Single crystals of electrically conductive two-dimensional metal–organic frameworks: structural and electrical transport properties. *ACS Cent. Sci.* **5**, 1959–1964 (2019).
23. Hmadeh, M. et al. New porous crystals of extended metal-catecholates. *Chem. Mater.* **24**, 3511–3513 (2012).
24. Dou, J.-H. et al. Atomically precise single-crystal structures of electrically conducting 2D metal–organic frameworks. *Nat. Mater.* **20**, 222–228 (2021).
25. Sun, L., Park, S. S., Sheberla, D. & Dincă, M. Measuring and reporting electrical conductivity in metal–organic frameworks: Cd_2(TTFTB) as a case study. *J. Am. Chem. Soc.* **138**, 14772–14782 (2016).
26. Ma, Y.-X. et al. Macrocycle-based metal–organic frameworks with NO_2-driven on/off switch of conductivity. *ACS Appl. Mater. Interfaces* **13**, 27066–27073 (2021).
27. Shang, X. et al. Chiral self-sorted multifunctional supramolecular biocoordination polymers and their applications in sensors. *Nat. Commun.* **9**, 3933 (2018).
28. Talin, A. A. et al. Tunable electrical conductivity in metal–organic framework thin-film devices. *Science* **343**, 66–69 (2014).
29. Lee, J. H., Jeoung, S., Chung, Y. G. & Moon, H. R. Elucidation of flexible metal–organic frameworks: research progresses and recent developments. *Coordin. Chem. Rev.* **389**, 161–188 (2019).
30. Xie, L. S. et al. Tunable mixed-valence doping toward record electrical conductivity in a three-dimensional metal–organic framework. *J. Am. Chem. Soc.* **140**, 7411–7414 (2018).
31. Mori, H., Yokomori, S., Dekura, S. & Ueda, A. Proton–electron-coupled functionalities of conductivity, magnetism, and optical properties in molecular crystals. *Chem. Commun.* **58**, 5668–5682 (2022).
32. Lim, D.-W. & Kitagawa, H. Proton transport in metal–organic frameworks. *Chem. Rev.* **120**, 8416–8467 (2020).
33. Xue, W.-L. et al. MOF-directed synthesis of crystalline ionic liquids with enhanced proton conduction. *Angew. Chem. Int. Ed.* **60**, 1290–1297 (2021).
34. Zhang, Y. et al. Sulfonate-functionalized polyoxovanadate-based metal–organic polyhedra for enhanced proton conduction via the synergy of linker and metal cluster vertex. *Chin. J. Struct. Chem.* **41**, 2208012–2208017 (2022).
35. Yan, F. Porous ionomers boosting the performances of proton exchange membrane fuel cells. *Sci. Bull.* **67**, 2505–2507 (2022).
36. Deng, W.-H. et al. A humidity-induced large electronic conductivity change of 10^7 on a metal–organic framework for highly sensitive water detection. *Angew. Chem. Int. Ed.* **62**, e202305977 (2023).
37. Park, S. S. et al. Cation-dependent intrinsic electrical conductivity in isostructural tetrathiafulvalene-based microporous metal–organic frameworks. *J. Am. Chem. Soc.* **137**, 1774–1777 (2015).
38. Narayan, T. C., Miyakai, T., Seki, S. & Dincă, M. High charge mobility in a tetrathiafulvalene-based microporous metal–organic framework. *J. Am. Chem. Soc.* **134**, 12932–12935 (2012).
39. Huang, J., Liu, F. & Zhang, J. Insights into adsorption rate constants and rate laws of preset and arbitrary orders. *Sep. Purif. Technol.* **255**, 117713 (2021).
40. Wang, H.-Y., Su, J. & Zuo, J.-L. Porous crystalline materials based on tetrathiafulvalene and its analogues: assembly, charge transfer, and applications. *Acc. Chem. Res.* **57**, 1851–1869 (2024).
41. Su, J. et al. High electrical conductivity in a 2D MOF with intrinsic superprotonic conduction and interfacial pseudo-capacitance. *Matter* **2**, 711–722 (2020).
42. Isono, T. et al. Hydrogen bond-promoted metallic state in a purely organic single-component conductor under pressure. *Nat. Commun.* **4**, 1344 (2013).
43. Ueda, A. et al. Hydrogen-bond-dynamics-based switching of conductivity and magnetism: a phase transition caused by deuterium and electron transfer in a hydrogen-bonded purely organic conductor crystal. *J. Am. Chem. Soc.* **136**, 12184–12192 (2014).
44. Lim, D.-W., Sadakiyo, M. & Kitagawa, H. Proton transfer in hydrogen-bonded degenerate systems of water and ammonia in metal–organic frameworks. *Chem. Sci.* **10**, 16–33 (2018).
45. Choi, J. Y. et al. 2D conjugated metal–organic framework as a proton-electron dual conductor. *Chem* **9**, 143–153 (2023).
46. Jo, Y.-M., Kim, D.-H., Wang, J., Oppenheim, J. J. & Dincă, M. Humidity-mediated dual ionic–electronic conductivity enables high

sensitivity in MOF chemiresistors. *J. Am. Chem. Soc.* **146**, 20213–20220 (2024).
47. Perdew, J. P. et al. Restoring the density-gradient expansion for exchange in solids and surfaces. *Phys. Rev. Lett* **100**, 136406 (2008).
48. Schimka, L., Harl, J. & Kresse, G. Improved hybrid functional for solids: The HSEsol functional. *J. Chem. Phys.* **134**, 024116 (2011).
49. Butler, K. T., Hendon, C. H. & Walsh, A. Electronic chemical potentials of porous metal–organic frameworks. *J. Am. Chem. Soc.* **136**, 2703–2706 (2014).

Acknowledgements

This work is supported by the Zhejiang Provincial Natural Science Foundation of China (XHD23B0301) and the Research Center for Industries of the Future (RCIF Project No. WU2023C006) at Westlake University. Computational aspects of this paper are supported by the National Science Foundation through the Division of Materials Research under grant no. DMR-1956403 and the Camille and Henry Dreyfus Foundation. We acknowledge Instrumentation and Service Center for Molecular Sciences and Instrumentation and Service Center for Physical Sciences at Westlake University as well as Westlake Center for Micro/Nano Fabrication for the facility support and technical assistance. We thank Prof. Qiyang Lu and Zihan Xu for helpful discussions and assistance with preliminary experiments. L.S. thanks Prof. Zhongyue Zhang and Prof. Sarah S. Park for helpful discussions. Y.W. thanks Yuan Cheng, Xu Chen, Dr. Fucheng Leng, Xin Li, Xi Mu, Dr. Yinjuan Chen, and Aimei Zhou at Westlake University for assistance with characterization and data analysis.

Author contributions

Y.W. conducted experiments. P.S.B. and C.H.H. performed band structure calculations. Y.W. and X.M. conducted X-ray crystallography. L.S. conceived the idea and oversaw the project. Y.W. and L.S. analyzed data, interpreted results, and co-wrote the manuscript.

Competing interests

The authors declare no competing interests.

Additional information

Supplementary information The online version contains supplementary material available at https://doi.org/10.1038/s43246-024-00620-2.

Correspondence and requests for materials should be addressed to Lei Sun.

Peer review information *Communications Materials* thanks the anonymous reviewer(s) for their contribution to the peer review of this work. Primary Handling Editor: Natalia Shustova and Jet-Sing Lee. A peer review file is available.